P2-Na0.67Mn0.85Al0.15O2 and NaMn2O4 Blend as Cathode Materials for Sodium-Ion Batteries Using a Natural β-MnO2 Precursor

John Abou-Rjeily, Ilham Bezza, Noureddine Ait Laziz, Daniela Neacsa, Cecile Autret-Lambert, Fouad Ghamouss

Article

P2-Na$_{0.67}$Mn$_{0.85}$Al$_{0.15}$O$_2$ and NaMn$_2$O$_4$ Blend as Cathode Materials for Sodium-Ion Batteries Using a Natural β-MnO$_2$ Precursor

John Abou-Rjeily, Ilham Bezza, Noureddine Ait Laziz, Daniela Neacsa, Cecile Autret-Lambert, and Fouad Ghamouss*

Cite This: *ACS Omega* 2021, 6, 1064−1072

Read Online

ACCESS | Metrics & More | Article Recommendations

ABSTRACT: Sodium-ion batteries (NIBs) are promising candidates for specific stationary applications considering their low-cost and cost-effective energetic property compared to lithium-ion batteries (LIBs). Additional cost cutbacks are achievable by employing natural materials as active cathode materials for NIBs. In this work, we report the use of natural pyrolusite (β-MnO$_2$) as a precursor for the synthesis of a NaMnO blend (a mixture of layered P2-Na$_{0.67}$Mn$_{0.85}$Al$_{0.15}$O$_2$ without any doping technique combined with a post-spinel NaMn$_2$O$_4$ without any high-pressure synthesis). The synthesized powder was characterized by XRD, evidencing these two phases, along with two additional phases. Tests for Na-ion insertion registered a reversible discharge capacity of 104 mA h/g after 10 cycles with a well-defined plateau at 2.25 V. After 500 cycles at a C/4 current density, a high Coulombic efficiency between 96 and 99% was achieved, with an overall 25% capacity retention loss. These pilot tests are encouraging; they provide economic relief since the natural material is abundant (low-cost). Desirable, energetic assurances and ecological confirmations are obtainable if these materials are implemented in large-scale stationary applications. The synthesis technique does not use any toxic metals or toxic solvents and has limited side product formation.
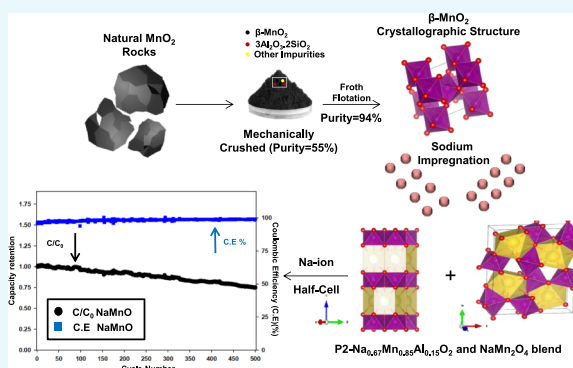
1. INTRODUCTION

The supremacy of rechargeable energy storage systems on modern science and technology is remarked through the ubiquitous implementation of these systems in devices we use daily. High-energy storage systems are functional in portable electronic devices (laptops and mobile phones), electric vehicles (hybrid or battery), and arrangements that harness renewable energy (wind turbines and solar panels). Lithium-ion batteries (LIBs) have dominated the rechargeable batteries market ever since their first commercialization by Sony Corp. in 1991.[1] The success of LIBs is due to the intensive research in this field and due to lithium's remarkable properties (lightest weight, high operating voltage, and excellent energy density).[2] However, due to their low abundance in the earth's crust (20 ppm) and uneven distribution (South America),[3] lithium metal and salts are considered to be costly, making their large-scale implementation expensive.

Instead, sodium-ion batteries (NIBs) are emerging as one of several significant candidates that might succeed LIBs owing to their high abundance in the earth's crust (23,600 ppm) and even distribution. Therefore, they might be more favored for large-scale applications due to their lower cost. Sodium salt via various electrolysis techniques can derive sodium metal, which has a lower unit value ($/ton) and higher production numbers

(tons) than lithium. The production of lithium reached its highest values in 2012 with 6.34×10^3 tons priced at 4400\$/ton, whereas that of sodium salt reached its maximum output in 2013 with 273×10^6 tons rated at 46\$/ton.[4] The production of sodium is a thousand times higher and cheaper than lithium.[4]

Moreover, aluminum operating as the anode current collector for NIBs is a cost-effective alternative of copper, further reducing the manufacturing cost.[5] Stationary application costs can also be reduced using natural resources as precursors to synthesize active cathode materials for LIBs and NIBs. Natural manganese oxide (pyrolusite-β-MnO$_2$) employed as a precursor provides further cost cutbacks since it is less costly compared to synthetic ones. Iron ore mining debris, such as manganese oxide, have been disregarded as waste materials. Thus, expending these materials ensures environmental realization while processing them by a solid-state

reaction to minimize their ecological impacts. It avoids chemical reagents for either purifying or mixing them with other components. Tarascon and Larcher highlighted several elements' sustainability, including manganese, since it can be naturally recycled.[6] Thus, manganese can deliver environmental guarantees for developing a sustainable and somehow greener battery. Furthermore, some advantages of solid-state reactions are the limited formation of side products and avoiding the use of solvents in the chemical reaction, further resolving waste disposal issues. Solid-state reactions are notified as "Green Chemistry," causing significant changes in the chemical synthesis of products.[7]

Na-ion intercalation-based oxide materials were primarily reported in the 1970s with various metals integrated into their structures (i.e., Na_xMO_2 where M is either cobalt, nickel, titanium, manganese, or other metals).[8,9] Most of these materials are both expensive and toxic. Nevertheless, manganese provides flawless cost cutbacks due to its availability and is a candidate to be realized in cathodes. A diversity of synthesized Na_xMnO_2 materials was reported with various synthesis techniques, forming diverse structures leading to altered electrochemical performances in terms of different energy storage techniques and different reversible capacities and stability. Generally, Na_xMnO_2 can be categorized into 2D and 3D structures depending on the Na (x) content ranging from 0.4 to 1.[10] An alternative categorization for Na_xMO_2 is based on the different ways of stacking the oxygen arrangement, wherever the Na^+ occupies the prismatic (P) or octahedral (O) sites between the MO_2 layers in a unit cell.[11] Na_xMnO_2 compounds face several challenges, especially in their ability to intercalate Na^+ (reversibly) over an extensive content range while attaining high energy density.[12]

One of the many Na_xMnO_2 compounds is $Na_{0.44}MnO_2$, with an orthorhombic crystal structure. It has attracted attention due to its large tunnel structure delivering a specific discharge capacity close to the theoretical value of 122 mA h/g.[13] On the other hand, $Na_{0.67}MnO_2$ achieves a higher specific capacity of 160 mA h/g (these P2-layered structures' theoretical capacity is 170 mA h/g). The $Na_{0.67}MnO_2$ demonstrates structural instability due to its tunnel system accompanied by Jahn–Teller distortion and manganese dissolution, leading to increased straining and distortions, which causes the host structure to collapse, yielding amorphous materials after eight cycles when cycled between 2 and 3.8 V at 0.1 mA/cm^2.[14,15] To resolve this problem, doping $Na_{0.67}MnO_2$ with aluminum to obtain P2-$Na_{2/3}Mn_{1-x}Al_xO_2$ (x varying between 1/18, 1/9, and 2/9), as reported by Wu et al., stabilizes the crystal lattice and prevents destructive Jahn–Teller distortion.[16] Alternatively, some reports discussed the possibility of synthesizing a post-spinel $NaMn_2O_4$, which has a theoretical capacity of 136 mA h/g when cycled between 2 and 4 V and a reversible capacity of 65 mA h/g at a current density of 5 mA/g (~C/27). However, these materials' synthesis techniques are carried out under high pressure (4.5 GPa).[17]

In this work, we report the use of natural raw pyrolusite (β-MnO_2) as starting materials to synthesize a composite NaMnO blend. The blend is a composite of layered P2-$Na_{0.67}Mn_{0.85}Al_{0.15}O_2$ (doping-free technique) and a post-spinel $NaMn_2O_4$ (pressure-free synthesis) via a simple synthesis technique. The method includes a solid-state reaction followed by a calcination process to produce a NaMnO blend tested as cathode materials in NIBs.

2. EXPERIMENTAL PROCEDURES

Natural manganese oxide rock was obtained from "Bou Tazoult" mine in the south of Morocco. This precursor's original purity was 55% identified by inductively coupled plasma mass spectrometry (ICP−MS). The MnO_2 was then purified via froth flotation, and the purity reached 94%. The ICP−MS test displayed the presence of aluminum, silicon, and sodium as impurities. The synthesis aimed to impregnate the natural manganese oxide with sodium using a sodium salt (Na_2CO_3). Synthesis parameters, such as the Na/Mn ratio, the calcination time, and pressure application, determine the end product's composition. Here, we report a simple synthesis route with a previously reported salt used in the synthesis of $Na_{0.44}MnO_2$.[18] Still, the calcination atmosphere was changed to the argon atmosphere without applying any pressure or vacuum. The natural precursor (β-MnO_2) was hand crushed and then mixed with sodium carbonate (Na_2CO_3) with a 4/1 ratio with an excess of 5% sodium salt, considering the volatility of sodium. The mixture was ball milled in an agate jar with several agate balls (1 cm diameter) at a speed of 350 rounds per minute for 5 h. After that, a calcination process at 700 °C for 10 h under an argon was held, producing a powder with a composition to be determined. The powders' phase purity and crystal structure were determined by X-ray diffraction (XRD) using an X-ray diffractometer (Bruker D8 Discover). The instrument provides a full-sized goniometer class powder (under ambient conditions) operating at 40 kV and 40 mA using Ni-filtered Cu Kα radiation (λ = 0.15406 nm). The data were recorded in the 2θ range of 10−90° at a scanning rate of 0.02 s/step. Diffraction pattern analysis/refinement was operated using the Fullprof program.

Scanning electron microscopy (SEM) imagery was coupled with energy-dispersive X-ray spectroscopy (EDS) analysis in a Samx machine. The Raman spectra were carried out using a "LabRam Hr Evolution" high spectral resolution laser Raman spectrometer. A small amount of powder was mounted on a glass lens and subjected to a green laser at 532 nm. Samples were tested using a 50× magnification lens. Angle-sensitive backscatter (AsB) was selected since a gray scale can be recognized, attributed to the Z-contrast, and thus allowing the distinction between low Z elements (such as carbon) and high Z elements (aluminum, silicon, and others). The Z-contrast demonstrates channeling contrast (crystallographic and strain information), hence some impurities show bright contrast (elements different from carbon which show darker contrast). Molecular schemes of the synthesized powder were drawn using VESTA software. Thermo-gravimetric analysis (TGA) was applied to the synthesized material at a 5 °C/min step under air and in a ceramic substrate at 800 °C to verify the water content of the blend and the continuous crystallization of the synthesized material.

Slurries prepared have a 60/30/10 ratio (active material, conductive carbon black, and polyvinylidene fluoride, respectively) with an N-methyl-2-pyrrolidone solvent. The high level of conductive carbon black taken into consideration is due to low electrical conductivity of some impurities. The slurry was prepared in an argon-filled glovebox with low oxygen content (<0.1 ppm) and water content (<3 ppm) to avoid any reaction of the powder with air, knowing that it is highly hygroscopic. These inks were deposited on aluminum films using a simple "doctor blade" technique delivering cathodes of 1.2−1.5 mg/cm^2 mass. The electrodes were then
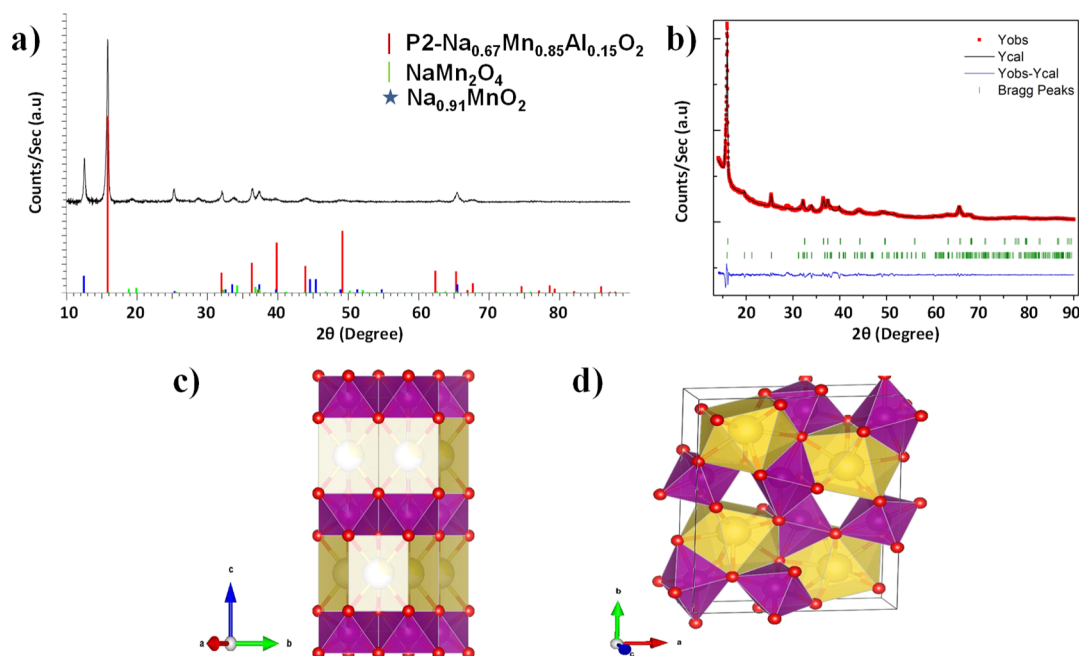
Figure 1. (a) XRD patterns of synthesized NaMnO blend, (b) XRD pattern analysis by Fullprof. Molecular scheme (c) $Na_{0.67}Mn_{0.85}Al_{0.15}O_2$ and (d) $NaMn_2O_4$ (Na is represented in yellow; Mn in purple; and O in red).

dried in a glovebox for 24 h and then cut and dried under vacuum for 4 h at 80 °C to remove residing water agglomerations. These electrodes were the working electrodes, whereas sodium metals were the counter and reference electrodes. The electrolyte utilized was composed of 1 M sodium hexafluorophosphate ($NaPF_6$) dissolved in propylene carbonate (PC) and fluoroethylene carbonate (FEC) with a 95/5 gravimetric ratio. A microporous fiberglass membrane was utilized as a separator between the electrodes (Whatman phase separators).

Electrochemical behaviors were studied by various tests, mainly cyclic voltammetry (CV) and galvanostatic cycling, with potential limitations (GCPL). A CV with a scan rate of ±0.025 mV/s projected into well-denoted voltammograms allowed the study of the behavior of electrodes/electrolyte interfaces and charge-transfer reactions.[23] In the GCPL tests, the cells were cycled between 2.0 and 4.0 V versus Na/Na^+ using various charge/discharge currents. Taking into consideration that each phase has a different theoretical capacity and operating voltages, the currents used were fixed based on the theoretical capacity of the more stable phases, that is, $NaMn_2O_4$.

3. RESULTS AND DISCUSSION

Expending natural precursors delivers a powder with a blend of phases rather than one phase since the material is not 100% pure. The XRD pattern of the synthesized blend is displayed in Figure 1a. Peak identification was made possible by implementing the EVA program showing three distinct phases. The main phase (87% of the composite) detected corresponds to a P2-type $Na_{0.67}Mn_{0.85}Al_{0.15}O_2$ phase (hexagonal unit, PDF no. 04-020-0008, space group $P6_3/mmc$), and its characteristic peaks are located around 16, 33, and 36° with a miller index of (002), (004), and (100), correspondingly represented by red dashes. The second phase is $NaMn_2O_4$ phase (3% of the composite) which has an orthorhombic unit cell with $Pnam$ as a space group with several characteristic peaks represented by

green dashes. The third phase, however, is an α-$Na_{0.91}MnO_2$ phase (9% of the composite) (O'3-type structure) represented by blue dashes, which is considered as an impure phase that was previously reported to exist in $Na_{2/3}Mn_{1-x}Al_xO_2$-doped materials, and as the aluminum content increases, these structures become less evident.[16] The last 1% of the composite is made up of other phases combining Na with various impurity components.

XRD analysis, as displayed in Figure 1b, shows two phases, one corresponding to $Na_{0.67}Mn_{0.85}Al_{0.15}O_2$ with the space group $P6_3/mmc$ and the other corresponding to $NaMn_2O_4$ with the space group $Pnma$. The final refinement is satisfactory, even if the peaks were not sharp, showing the existence of defects in the materials. The reliability factors are R_p: 4.42%, R_{wp}: 6.04%, and χ^2: 4.69. The R_{bragg} are respectively equal to 1.4% for phase 1 and 1.8% for phase 2.

The schematic representation of the first phase ($Na_{0.67}Mn_{0.85}Al_{0.15}O_2$), shown in Figure 1c, describes the hexagonal symmetry in the space group $P6_3/mmc$ with the presence of layer spaces permit facile intercalation/deintercalation of Na^+. The crystal structure of P2-$Na_{0.67}Mn_{0.85}Al_{0.15}O_2$ represents an ABBA-type oxide-ion layer stacking.[19] Sodium ions occupy two prismatic sites, while manganese ions occupy an octahedral site (MnO_6). On the other hand, the schematic representation of $NaMn_2O_4$ (Figure 1d) indicates a lower symmetry and reduced occupied sites, which are a drawback in the Na ion intercalation/de-intercalation process. Meanwhile, the $NaMn_2O_4$ shows a 3D framework structure with tunnels formed by four vertex sharing chains. Mainly, two MnO_6 octahedrons share edges to create a chain, and they are connected to adjacent ones by sharing vertices. Significantly, all sodium ions are located in the tunnels, providing reversible charging/discharging processes.[17]

The pyrolusite powder is less homogenous compared to the synthesized NaMnO blend since the latter was ball milled during the preparation process producing a more homogenous powder with equally sized flakes. The flake size after synthesis
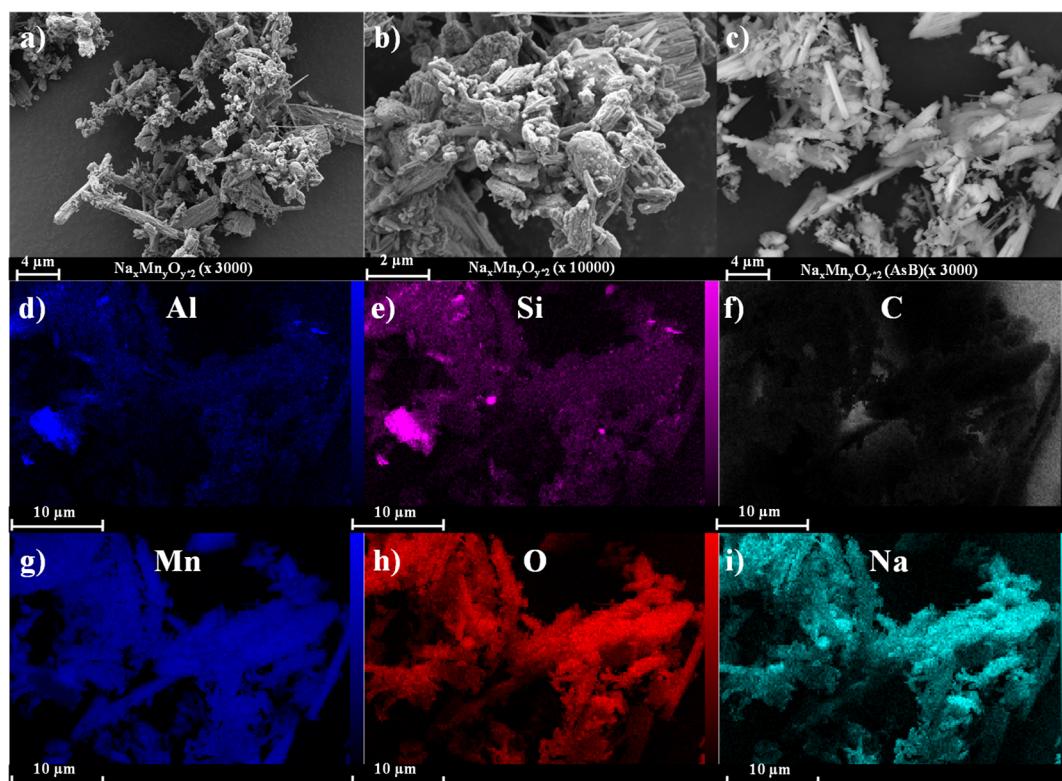
Figure 2. SEM imagery of NaMnO powder: (a) x3k and (b) x10k; AsB of NaMnO (c) x3k. EDS frame analysis of NaMnO: (d) Al, (e) Si, (f) C, (g) Mn, (h) O, and (i) Na.

ranges between ∼3 and 33 μm with particle size smaller than the natural raw pyrolusite along with the presence of fissures and cracks, especially for large particle-sized, which could be considered as a direct consequence of the synthesis process, as shown in Figure 2a.

SEM images of the powder at a 10k magnification (Figure 2b) showed that the NaMnO blend is covered with a layer making the surface rougher than the β-MnO$_2$ due to the sodium salt used in the process. AsB imagery for the synthesized powder displayed a gray-scale frame, with the majority of the image being high in contrast due to the presence of high Z elements (Figure 2c). EDS mapping analysis of the β-MnO$_2$ showed similar elements in comparison with the NaMnO blend except for the existence of sodium (Na) after synthesis, which was absent in the raw powder and present in the synthesized powder, further emphasizing the success of sodium impregnation into the MnO$_2$ matrix (Figure 2i).

Elements such as aluminum, silicon, carbon, manganese, and oxygen were also detected by EDS mapping for both the raw pyrolusite and the synthesized blend. The presence of these elements was expected and can be attributed to the natural origin of the precursor. Due to its natural sources, the natural pyrolusite is expected to contain aluminum oxide (Al$_2$O$_3$) and silicon oxide (SiO$_2$). The silicon and aluminum coexisted in similar areas. Owing to their natural origins, compounds such as mullite (3Al$_2$O$_3$·2SiO$_2$) are evident in these materials. These elements' presence is unique to natural products and could be of electrochemical significance in NIB cathodes.[20]

Structural alterations were expected after the synthesis of the NaMnO blend. Raman scattering further confirms this supposition since it displayed peaks and shifts different from that of the natural precursor and the sodium salt used

(Na$_2$CO$_3$). As shown in Figure 3, the Raman spectrum of the NaMnO blend demonstrates a dominant peak at ∼645 cm^{-1} in
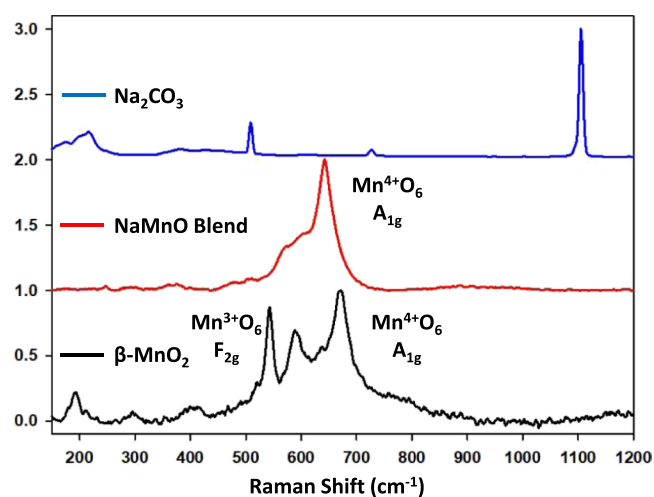
Figure 3. Raman spectra of natural pyrolusite (black), NaMnO blend (red), and Na$_2$CO$_3$ (blue).

coherence with past research.[21] This peak is attributed to the A$_{1g}$ mode of stretching vibration of the MnO$_6$ group in sodium manganese oxide. Several smaller peaks were also detected at ∼510, ∼376, and 247 cm^{-1}, which resemble E$_{2g}$ and E$_{1g}$ symmetries. It is worth noting that the shoulder at ∼580 cm^{-1} is not well separated from the 625 cm^{-1} peak due to its low intensity; it is also speculated that this shoulder is closely related to the average oxidation state of manganese oxide in the spinal phase.[22] The spinal phase peaks were not reported in

the literature, and due to their similar chemical nature to $Na_{0.67}MnO_2$, it is suggested that they display similar peaks and vibration patterns. The absence of several peaks compared to the raw precursor indicates that the synthesized powder attains different vibration modes and reports the success in changing the powder's state.

TGA characterization of the synthesized blend displayed water loss and a reaction of one of the blend's components with excess salts. The TGA curve displayed a multi-step weight loss due to increasing temperatures (up to 800 °C). First, it is noticeable that the synthesized blend has a different TGA profile compared to the raw pyrolusite (Figure 4). The first
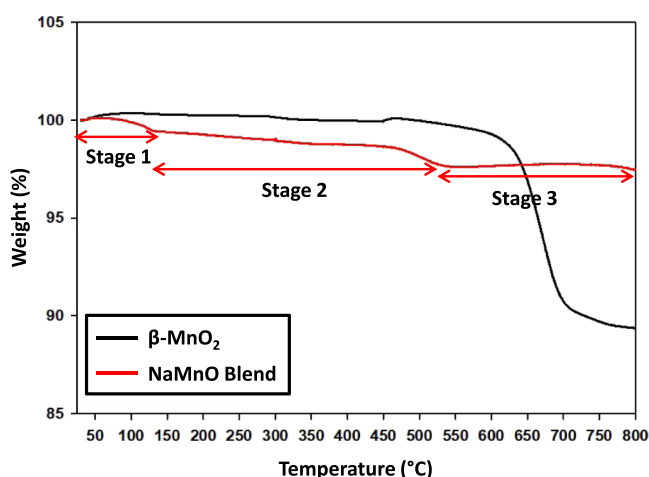
Figure 4. TGA of (a) natural pyrolusite (black) and NaMnO blend (red) with their designated weight loss as a function of temperature.

step resembles water loss removed from the surface up to 150 °C (stage 1), adding up to 0.7 wt % loss in the overall weight. The water content in the material originated from the synthesized blend's nature, which is considered to be hygroscopic.[1] Compared to the literature, the NaMnO blend displays a 4 wt % weight loss,[23] whereas Na-Bir shows an 8 wt % weight loss of surface water.[24] During the second stage, weight loss takes place up to 500 °C, resembling a reaction of Na_2CO_3 with $Na_{0.67}MnO_2$, as shown in the following equation

$$Na_{0.67}MnO_2 + 1/6Na_2CO_3$$

$$\rightarrow NaMnO_2 + 1/6CO_2 + 1/12O_2 \qquad (1)$$
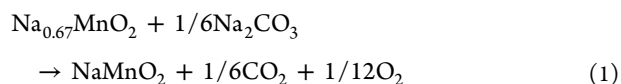
During this stage, the total weight loss was 1.2% compared to the literature (~1 to 1.5%).[23] If $Na_{0.67}MnO_2$ further reacts with Na_2CO_3, in theory, the weight loss should be ≥8.6 wt % (i.e., to attain $NaMnO_2$), whereas for the synthesized blend, the recorded weight loss was ~0.7 wt %, which further confirms the mixed state of the synthesized powder (i.e., $Na_{0.67}Mn_{0.85}Al_{0.15}O_2$ and $NaMn_2O_4$). This weight loss can be attributed to the carbon combustion unmasked by other reactions. The synthesis of the powder was under an argon, and carbon combustion did not take place.

The synthesized NaMnO blend porosity and textural properties were measured through the N_2 adsorption method using a QUADRASORB EVO apparatus using quenched solid-state functional theory (QSDFT), revealing the cumulative pore volume and pore size distribution. The BET model was also realized since it serves to measure the specific surface area of materials in theory. The cumulative pore volume of the synthesized sample showed a reduced value compared to that of the raw pyrolusite (Figure 5). It was noticed that micropores were absent for both samples and that both powders are considered to be mesoporous (pore size >2 nm). Minor differences in the small mesopores were recorded for the synthesized blend. The inset (Figure 5a) demonstrates the volume contribution of these pores (between 2 and 4 nm) formed after thermal calcination. Mesopores of larger width/diameter (>4 nm) were also recorded, and since they are larger, they majorly contributed to the overall cumulative volume. Moreover, pore size distribution further validates these observations, where a peak at ~4.2 nm was noticed for the synthesized powder. In contrast, a peak at ~4.5 nm was detected for the raw pyrolusite (Figure 5b). The inset demonstrates the absence of this peak in the raw pyrolusite. Mesopores distribution was further detected, with several peaks recorded between 4 and 36 nm. It was noticed that each signal of the peaks was divided into two smaller peaks, whether at ~4.5 or ~7.5 nm, as a direct consequence of the synthesis technique (ball milling and calcination).

Data derived from QSDFT and BET models are summarized in Table 1. Distinctions were made regarding the volume distribution per pore size, cumulative pore volume,
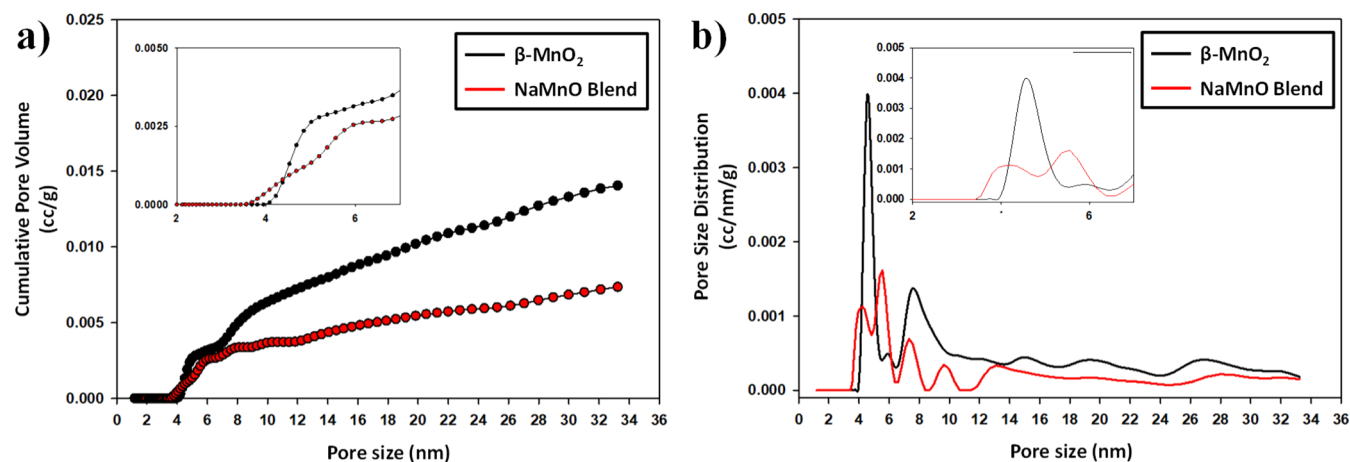
Figure 5. (a) Cumulative pore volume and (b) pore size distribution of β-MnO_2 (black) and NaMnO blend (red). Insets display the previous values over a pore size range of 2−7 nm.

Table 1. QSDFT and BET-Derived Data of Samples before and after Synthesis

| sample	specific surface area (m²/g)	cumulative pore volume (cc/g)	pore width (nm)	$V_{(<2\ nm)}$ (%)	$V_{(2-4\ nm)}$ (%)	$V_{(4-10\ nm)}$ (%)	$V_{(>10\ nm)}$ (%)
β-MnO$_2$	24.9	0.014	4.5	0	0	50	50
NaMnO blend	4.8	0.007	5.5	0	4.3	46	49.7
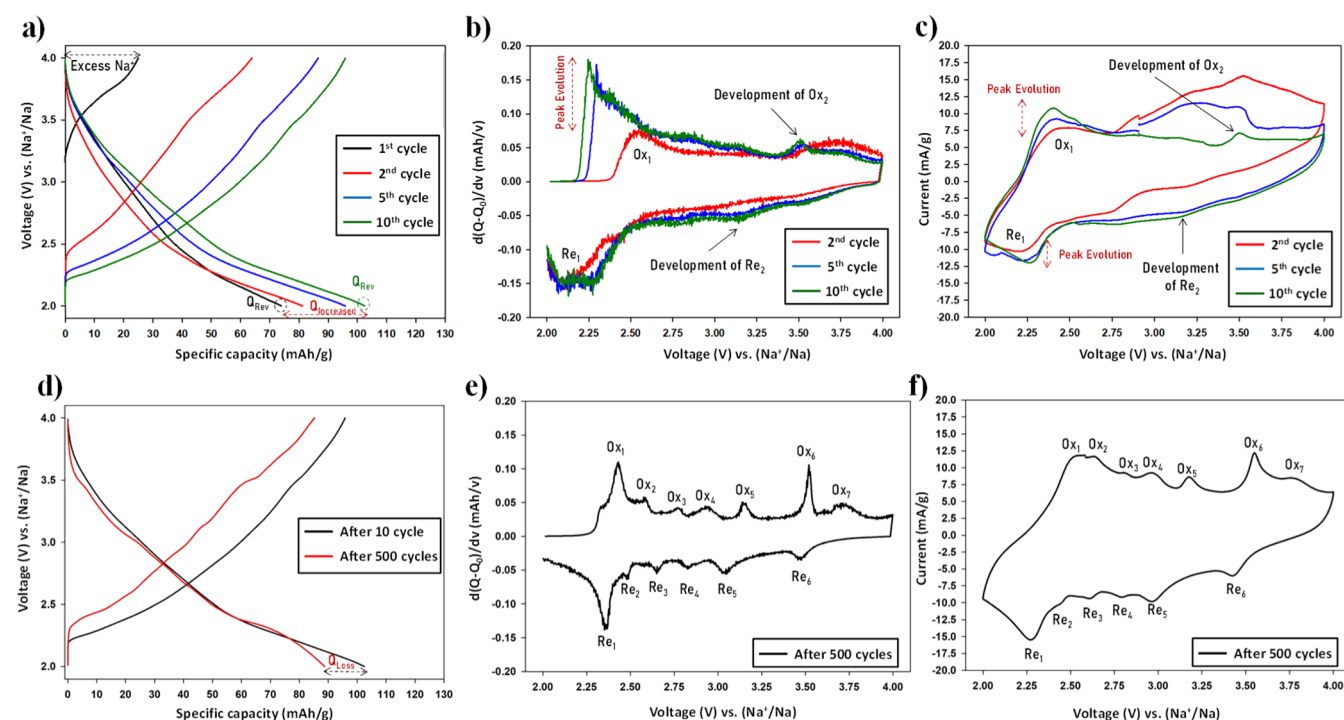
Figure 6. Electrochemical characterization of the NaMnO blend with PC/FEC (95:5) + 1 M LiPF$_6$ vs Na. The first 10 cycles: (a) GCPL at C/20, (b) differential capacity (dQ/dV vs E), (c) CV and after 500 cycles, (d) GCPL at C/20, (e) differential capacity (dQ/dV vs E), and (f) CV.

pore width, and specific surface area. During the synthesis of NaMnO blend powder, thermal calcination leads to crystal growth, hence decreasing the specific surface area from 24.9 to 4.8 m²/g. As reported in the literature, this crystal growth causes several pores' shutdown, thus attaining lower cumulative volume (decrease from 0.014 to 0.007 cc/g).[25] However, the increased pore width seems promising for cycling Na$^+$ into the synthesized materials. As shown in Table 1, micropores are absent in both samples. Nevertheless, small-sized mesopores (2−4 nm) were absent in the raw pyrolusite. Whereas, in the synthesized NaMnO blend, they contributed to 4.3% of the total volume. Larger mesopores (4−10 nm) were more evident in raw pyrolusite (50% of the total volume). They added up to 0.007 cc/g of the total cumulative volume compared to the synthesized NaMnO blend (∼0.003 cc/g). The mesopores ranging from 10 to 36 nm were the most marked in both samples, but they contributed to 0.007 cc/g of the total volume for the raw pyrolusite. In contrast, they contributed to half of that volume for the synthesized NaMnO blend. Comparison with the previous literature reports proved to be difficult due to the powder's unique blend and the rarity of porosity studies regarding sodium-doped manganese oxide cathode materials.

The electrochemical behavior was initiated with galvanostatic cycling (Figure 6a) of the formulated cathodes in half cells displaying a unique performance. Charging from the OCV (desodiation) to 4 V at a C/20 versus Na$^+$/Na showed that Na$^+$ intercalation exceeds that of deintercalation. Considering that the NaMnO blend is majorly made up of Na$_{0.67}$Mn$_{0.85}$Al$_{0.15}$O$_2$ (∼86%), the argument of Na$^+$ intercala-

tion will be based on this component. Nonetheless, the presence of post-spinal NaMn$_2$O$_4$ (∼3%) and its electrochemical contribution is considered to be minor; however, its role in stabilizing the blend cannot be neglected. Pointing out that the theoretical capacity of Na$_{0.67}$MnO$_2$ is 170 mA h/g, but since the material is an impure blend, we fixed the 1C charge/discharge rate at 100 mA/g (which should ≜ 0.67 Na$^+$). The first charge capacity was 25 mA h/g (≜ 0.098 Na$^+$ deintercalated), indicating the residue of 0.572 Na$^+$ in the blend's crystal lattice. The previous observation indicates that the overall blend contained >1/3 of the Na content residing in its lattice, which is crucial for this P2-layered structure's stability.[26] Meanwhile, the sodiation (discharge to 2 V) displays a specific discharge capacity of 74 mA h/g, which corresponds to the intercalation of 0.295 Na$^+$ (Na$^+$ content in the blend is 0.875). However, the subsequent sodiation displayed a 64 mA h/g (≜ to 0.252 Na + deintercalation) charge capacity, that is, 85% of the total intercalated Na$^+$ of the first intercalation cycle. Thus, it is supposed that the other 15% resided in the crystal lattice. Similar behaviors occurred during the subsequent cycles, where the discharge capacity kept increasing until the 10th cycle, where it reached 104 mA h/g (i.e., 44% overall increase). Compared to the post-spinel NaMn$_2$O$_4$, the discharge capacity is higher by 60%.[17] Nonetheless, it is lower than the discharge capacity of Al$_2$O$_3$-doped Na$_{0.67}$MnO$_2$[27] and P2-Na$_{2/3}$Mn$_{1-x}$Al$_x$O$_2$[16] by 31 and 37%, respectively. Considering that the blend is made up of 83% P2-Na$_{0.67}$Mn$_{0.85}$Al$_{0.15}$O$_2$ and that the raw material is impure, the reversible capacity is lower than the ones reported
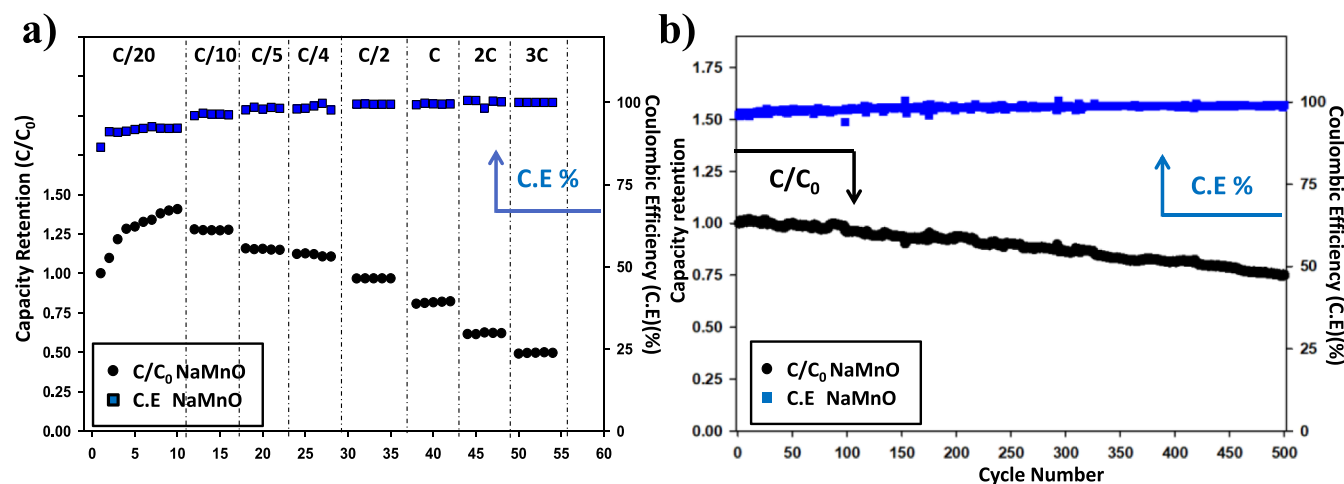
Figure 7. Additional electrochemical characterization of NaMnO blend with PC/FEC (95:5) + 1 M LiPF$_6$ vs Na: (a) rate capability up to 3C and (b) relative capacity retention and Coulombic efficiency at C/4 vs Na.

in the previous literature. It is worth noting that the Coulombic efficiency recorded in these initial cycles follows an unusual pattern (>100%) proposed to be linked to the cathode activation (stabilizing the lattice by intercalating Na$^+$) during these initial cycles as the discharge capacity was augmenting.

Monitoring the peak position recorded in the galvanostatic cycling was made possible by monitoring the differential capacity versus voltage (dQ/dV vs E) (Figure 6b) and by CV (Figure 6c). Two noticeable oxidation and reduction peaks were recorded. One redox couple occurs at low potentials, whereas the other occurs at high potentials. Noticeably, the redox peak at higher potentials is shifting to lower potentials. The de-evolution of a broad peak into a higher intensity peak at high potentials (∼3.5 V) was observed (Figure 6b). Due to the high overpotential during the first cycle, the peak position is not representative and thus not demonstrated in the figure. During the second cycle, an oxidation peak at ∼2.5 V was recorded, representing a plateau's start in the GCPL. The broad peak between 3.5 and 4 V was recorded, resembling the small plateau evident in the GCPL during the charge cycle at these potentials. During discharge, the quantity of charge was increasing, and a well-defined reduction peak was observed between 2.5 and 2 V. These low potential redox peaks represent the Mn^{3+}/Mn^{4+} redox reactions owing to the intercalation of Na$^+$, a matter also reported in the literature.[28] Upon cycling, the oxidation peaks increase in intensity. They are displaced to lower potentials showing that oxidation reactions start at lower potentials and decreased polarization (as the charge/discharge curve in the GCPL demonstrates a plateau at lower potentials). Also, the narrowing of the oxidation peak at ∼3.5 V is more evident after 10 cycles. The narrowing of the peaks shows the absence of Jahn−Teller distortion.[14] The shift of the peaks (representing several electrochemical reactions) indicates decreased polarization resistance due to the electrode's activation. It was noticeable that the peaks' narrowing was coupled with oxidation/reduction peak position shifts into more symmetrical positions. During the reduction reactions, multi-step peaks were more evident with a further increase in the quantity of charge, resembling increased discharge capacity (sodiation).

This matter was further discussed in the CV (Figure 6c). Previous annotations regarding the broad oxidation peak at

∼3.5 V were reported with its narrowing upon cycling and the increase of the delivered current recorded at ∼2.5 V with further narrowing of the peak. During these initial cycles, it is suggested that the Na$_{0.67}$Mn$_{0.85}$Al$_{0.15}$O$_2$ role in terms of electrochemical reactions was not evident.

During the initial cycles, the GCPL follows a semi-smooth charge−discharge profile typical of Na$_{2/3}$Mn$_{1−x}$Al$_x$O$_2$,[16] as displayed in Figure 6d (black), rather than the smooth profile of post-spinal NaMn$_2$O$_4$[17] and Al$_2$O$_3$-doped Na$_{0.67}$MnO$_2$.[27] However, the reversible capacity recorded for these Al-doped cathodes reached ∼150 mA h/g, values significantly higher, and a post-spinel NaMn$_2$O$_4$ ∼65 mA h/g is substantially lower than those of the synthesized blend. The multi-step curves were noticed after 500 cycles (stability and capacity retention tests), as displayed in Figure 6d (red). The differential capacity of the GCPL after the stability test shows several reversible oxidation/reduction peaks, as shown in Figure 6e. These peaks' profile is well defined with a significant ox/red peak at low voltages, representative of the Mn^{3+}/Mn^{4+} oxidation−reduction reactions. At higher voltages (i.e., from 2.5 to 3.25 V), additional four ox/red peaks (ox/red peak 2, 3, 4, and 5) were noticed with equivalent differential capacity values, further validating the high reversibility of the phase transitions occurring in this blend. Nonetheless, redox peak #6 shows unequal capacities, which might explain the capacity fading witnessed during the stability test; oxidation peak #7 has no equivalent intense reduction peak. We hypothesize that this reaction's irreversibility is related to an irreversible phase transformation; however, an extensive/broad profile was noticed, as displayed in the CV (Figure 6f). These peaks represent the stepwise intercalation of Na$^+$ into the P2-structured Na$_{0.67}$MnO$_2$.[27] The CV profile further confirms that previous annotations were complementary peaks. It is worth noting that typical Na$_{0.67}$MnO$_2$ profiles are multi-step curves accompanied by excessive phase transitions, which are usually irreversible.

As the voltammograms display, the multi-step sweeps with several oxidation−reduction peaks suggest that the electrochemical reactions of P2-structured Na$_{0.67}$Mn$_{0.85}$Al$_{0.15}$O$_2$ mask the electrochemical contribution of the post-spinel NaMn$_2$O$_4$ and the latter is the main electrochemical contributor. However, Na$_{0.67}$MnO$_2$ cathode materials displaying a multi-

step profile were reported to have low stability, and thus checking for the stability of this blend was necessary.

The rate capability of NaMnO blend-based cathodes was performed at various current densities ranging from C/20 to 3C in the potential range of 2 to 4 V. The specific discharge capacity, as discussed previously, was increasing until the 10th cycle recording a sodiation capacity of 104 mA h/g. As the current density increases, the discharge capacity decreases to lower values. The discharge capacity drop relating to kinetic limitations was witnessed (e.g., at C/10 = 94 mA h/g and C/2 = 72 mA h/g).

The capacity recorded at different charge/discharge rates up to 3C showed that the active material loses more than half of its capacitive capability at 2C (Figure 7a). The capacity losses after high-rate cycling arise from kinetically limited phase transformation. Nevertheless, lowering the current density back to the equivalent of a C/20 showed that the reversible capacity recovered was 102 mA h/g, that is, 98% capacity recovery (of the 10th cycle). Hence, the overall manganese dissolution and original capacity loss after rate capability tests (50 cycles at different currents) were 2% attributed to manganese dissolution from the blend structure. This active material's capabilities to cycle at different rates and recover 98% of its original capacity prove to be interesting, taking into consideration that the initial precursor is natural and contains impurities.

Furthermore, after rate capability, the cell was further cycled for an additional 500 cycles at a C/4 current to evaluate its long-term stability. Figure 7b shows that the capacity retention (as displayed by C/C_0) is 0.75, corresponding to a 25% overall capacity fade after >500 cycles. The Coulombic efficiency (i.e., charge/discharge capacity) reports values between 96 and 99%, indicating a very good reversible Na^+ intercalation/deintercalation. The previous set of information suggests that the spinel structure and the aluminum oxide present in the material enhance cycling stability. They also indicate that impurities' presence does not affect the material's performance since it can be cycled at different rates with minor capacity fade and high Coulombic efficiency, suggesting that manganese dissolution is minute in the first 100 cycles. However, the impact of impurity influenced the specific capacity.

Noticeably, after rate capability and stability tests, an additional electrochemical test was carried out, that is, cycling at C/20 again to verify the total manganese dissolution (Figure 6d). This test showed a discharge capacity of 85 mA h/g, that is, ~81% of the highest discharge capacity obtained during the 10th cycle. Thus, after the capacity retention test and the stability test at C/4, the overall capacity fade was 19%. Overall, the NaMnO-based electrode showed high stability after 100 cycles and after cycling at different rates. It is suggested that after a certain number of cycles, the cycling of the NaMnO blend becomes more active. The electrode's stability may be due to the presence of natural contributors such as aluminum oxide and/or the post-spinel structures preventing the collapse of these systems.

4. CONCLUSIONS

Natural pyrolusite in energy storage systems was neither assessed in the raw state nor in the modified/purified states. The crystallographic structure of this precursor was detected by XRD (i.e., β-MnO_2). Additional physico-chemical analysis suggested a weak electrochemical capability due to the large flake size, small tunnel size, low surface area, and cumulative volume of the raw materials. However, the use of this natural pyrolusite as a precursor in the synthesis of cathode materials to be implemented in NIBs proved to be valuable and delivered financial and energetic assurances. Solid-state synthesis techniques ensured the economic and environmental guarantee, especially that solvent use was absent, and since manganese by its nature is a low-cost material. The formulation of a unique blend (NaMnO blend) by a solid-state reaction followed by a calcination process is reported. The synthesized material consists of a mixture of several phases with different sodium contents and other structures. The coexistence of the two phases and their synergy (P2-$Na_{0.67}Mn_{0.85}Al_{0.15}O_2$ and $NaMn_2O_4$) is the main contributor to the blend material's overall electrochemical performance. The application of these materials in cathodes and tested in NIBs showed a remarkable electrochemical performance where the delivered discharge capacity increased (from 64 to 104 mA h/g) during the early cycles and stabilized with insignificant manganese dissolution after 100 cycles (~0.02%) and after more than 500 cycles (~19%). Each phase in this blend played substantial roles, either stabilizing the structure ($NaMn_2O_4$) or delivering enhanced discharge capacity (P2-$Na_{0.67}Mn_{0.85}Al_{0.1}O_2$). The presence of impurities had no impact on the electrochemical stability; on the contrary, it is suggested that some of them have beneficial roles further stabilizing this active material. This work shows the possibility of using these natural precursors. Nevertheless, further studies concerning each phase's role and surveying the effect of the synthesis parameters are necessary. Finally, it is worth noting that several experiments can be carried out in future, such as intentionally doping a "pure phase" NaMnO cathode materials with mullite, removing the impurities from the synthesized phase, and starting the same synthesis but with different precursors or at different temperatures.

■ AUTHOR INFORMATION

Corresponding Author

Fouad Ghamouss − *Laboratoire de Physico-Chimie des Matériaux et des Electrolytes pour l'Energie (PCM2E), Université de Tours, Tours 37020, France;* orcid.org/0000-0002-2419-0385; Phone: +33-061-075-6361; Email: Ghamouss@univ-tours.fr

Authors

John Abou-Rjeily − *Laboratoire de Physico-Chimie des Matériaux et des Electrolytes pour l'Energie (PCM2E), Université de Tours, Tours 37020, France*

Ilham Bezza − *Laboratoire de Physico-Chimie des Matériaux et des Electrolytes pour l'Energie (PCM2E), Université de Tours, Tours 37020, France*

Noureddine Ait Laziz − *Faculté des Sciences, Laboratoire de Physique du Solide et des Couches Minces (LPSCM), Université Cadi Ayyad, Marrakech 40032, Morocco*

Daniela Neacsa − *Faculté des Sciences, Groupe de Recherche en Matériaux, Microélectronique, Acoustique et Nanotechnologies (GREMAN), Université de Tours, Tours 37020, France*

Cecile Autret-Lambert − *Faculté des Sciences, Groupe de Recherche en Matériaux, Microélectronique, Acoustique et Nanotechnologies (GREMAN), Université de Tours, Tours 37020, France; Department of Materials Science, Energy, and Nano-engineering, Mohamed VI Polytechnic University, Ben Guerir, Morocco*

Complete contact information is available at:
https://pubs.acs.org/10.1021/acsomega.0c01647

Notes

The authors declare no competing financial interest.

■ REFERENCES

(1) Kubota, K.; Komaba, S. Review—Practical issues and future perspective for Na-ion batteries. *J. Electrochem. Soc.* **2015**, *162*, A2538−A2550.

(2) van Schalkwijk, W.; Scrosati, B. Advances in lithium-ion batteries introduction. *Adv. Lithium-Ion Batteries* **2002**, 1−5.

(3) Yabuuchi, N.; Kubota, K.; Dahbi, M.; Komaba, S. Research development on sodium-ion batteries. *Chem. Rev.* **2014**, *114*, 11636−11682.

(4) Kelly, T. D.; Matos, G. R., Historical statistics for mineral commodities in the United States (2016 version). US Geol. Surv. Data Ser., 2014, Vol. *140*. https://minerals.usgs.gov/minerals/pubs/historical-statistics/ (accessed Jan 24, 2019).

(5) Hwang, J.-Y.; Myung, S.-T.; Sun, Y.-K. Sodium-ion batteries: present and future. *Chem. Soc. Rev.* **2017**, *46*, 3529−3614.

(6) Larcher, D.; Tarascon, J.-M. Towards greener and more sustainable batteries for electrical energy storage. *Nat. Chem.* **2015**, *7*, 19−29.

(7) Cave, G. W. V.; Raston, C. L.; Scott, J. L. Recent advances in solventless organic reactions: Towards benign synthesis with remarkable versatility. *Chem. Commun.* **2001**, *21*, 2159−2169.

(8) Tarascon, J.; Hull, G. W. Sodium intercalation into the layer oxides $Na_xMo_2O_4$. *Solid State Ionics* **1986**, *22*, 85−96.

(9) Slater, M. D.; Kim, D.; Lee, E.; Johnson, C. S. Sodium-ion batteries. *Adv. Funct. Mater.* **2013**, *23*, 947−958.

(10) Han, M. H.; Gonzalo, E.; Singh, G.; Rojo, T. A comprehensive review of sodium layered oxides: Powerful cathodes for Na-ion batteries. *Energy Environ. Sci.* **2015**, *8*, 81−102.

(11) Delmas, C.; Fouassier, C.; Hagenmuller, P. Structural classification and properties of the layered oxides. *Phys. B+C.* **1980**, *99*, 81−85.

(12) Yu, L.; Wang, L. P.; Liao, H.; Wang, J.; Feng, Z.; Lev, O.; Loo, J. S. C.; Sougrati, M. T.; Xu, Z. J. Understanding fundamentals and reaction mechanisms of electrode materials for Na-ion batteries. *Small* **2018**, *14*, 1−22.

(13) Zhou, X.; Guduru, R. K.; Mohanty, P. Synthesis and characterization of $Na_{0.44}MnO_2$ from solution precursorsr. *J. Mater. Chem. A* **2013**, *1*, 2757.

(14) Caballero, A.; Hernán, L.; Morales, J.; Sánchez, L.; Santos Peña, J.; Aranda, M. A. G. Synthesis and characterization of high-temperature hexagonal $P2-Na_{0.6}$ MnO_2 and its electrochemical behaviour as cathode in sodium cells. *J. Mater. Chem.* **2002**, *12*, 1142−1147.

(15) Kim, S.; Ma, X.; Ong, S. P.; Ceder, G. A comparison of destabilization mechanisms of the layered Na_xMO_2 and Li_xMO_2 compounds upon alkali de-intercalation. *Phys. Chem. Chem. Phys.* **2012**, *14*, 15571−15578.

(16) Pang, W.-L.; Zhang, X.-H.; Guo, J.-Z.; Li, J.-Y.; Yan, X.; Hou, B.-H.; Guan, H.-Y.; Wu, X.-L. P2-type $Na_{2/3}Mn_{1-x}Al_xO_2$ cathode material for sodium-ion batteries: Al-doped enhanced electrochemical properties and studies on the electrode kinetics. *J. Power Sources* **2017**, *356*, 80−88.

(17) Liu, X.; Wang, X.; Iyo, A.; Yu, H.; Li, D.; Zhou, H. High stable post-spinel $NaMn_2O_4$ cathode of sodium ion battery. *J. Mater. Chem. A* **2014**, *2*, 14822−14826.

(18) Zhao, L.; Ni, J.; Wang, H.; Gao, L. $Na_{0.44}MnO_2$-CNT electrodes for non-aqueous sodium batteries. *RSC Adv.* **2013**, *3*, 6650−6655.

(19) Clément, R. J.; Bruce, P. G.; Grey, C. P. Review—Manganese-based P2-type transition metal oxides as sodium-ion battery cathode materialsr. *J. Electrochem. Soc.* **2015**, *162*, A2589−A2604.

(20) Han, D.-W.; Ku, J.-H.; Kim, R.-H.; Yun, D.-J.; Lee, S.-S.; Doo, S.-G. Aluminum manganese oxides with mixed crystal structure: high-energy-density cathodes for rechargeable sodium batteries. *Chem-SusChem* **2014**, *7*, 1870−1875.

(21) Sendova-Vassileva, M.; Stoyanova, R.; Carlier, D.; Yoncheva, M.; Zhecheva, E.; Delmas, C. Raman spectroscopy study on $Na_{2/3}Mn_{1-x}Fe_xO_2$ oxides. *Adv. Sci. Technol.* **2010**, *74*, 60−65.

(22) Ramana, C. V.; Massot, M.; Julien, C. M. XPS and Raman spectroscopic characterization of $LiMn_2O_4$ spinels. *Surf. Interface Anal.* **2005**, *37*, 412−416.

(23) Ma, T.; Xu, G.-L.; Zeng, X.; Li, Y.; Ren, Y.; Sun, C.; Heald, S. M.; Jorne, J.; Amine, K.; Chen, Z. Solid state synthesis of layered sodium manganese oxide for sodium-ion battery by in-situ high energy X-ray diffraction and X-ray absorption near edge spectroscopy. *J. Power Sources* **2017**, *341*, 114−121.

(24) Li, Y.; Feng, X.; Cui, S.; Shi, Q.; Mi, L.; Chen, W. From α-$NaMnO_2$ to crystal water containing Na-birnessite: enhanced cycling stability for sodium-ion batteries. *CrystEngComm* **2016**, *18*, 3136−3141.

(25) Malloy, A. P.; Donne, S. W. Porosity changes during reduction of γ-MnO_2 for aqueous alkaline applications. *J. Electrochem. Soc.* **2008**, *155*, A817.

(26) Sharma, N.; Tapia-Ruiz, N.; Singh, G.; Armstrong, A. R.; Pramudita, J. C.; Brand, H. E. A.; Billaud, J.; Bruce, P. G.; Rojo, T. Rate dependent performance related to crystal structure evolution of $Na_{0.67}Mn_{0.8}Mg_{0.2}O_2$ in a sodium-ion battery. *Chem. Mater.* **2015**, *27*, 6976−6986.

(27) Luo, C.; Langrock, A.; Fan, X.; Liang, Y.; Wang, C. P2-type transition metal oxides for high performance Na-ion battery cathodes. *J. Mater. Chem. A* **2017**, *5*, 18214−18220.

(28) Hou, Z.; Li, X.; Zhu, Y.; Liang, J.; Qian, Y. An aqueous rechargeable sodium ion battery based on a $NaMnO_2 −NaTi_2(PO_4)_3$ hybrid system for stationary energy storage. *J. Mater. Chem. A* **2014**, *3*, 1400−1404.